Frontiers in Heat and Mass Transfer

Tech Science Press

https://doi.org/10.32604/fhmt.2026.083846

ARTICLE

Experimental Study of the Effects of Surface Structure on Frosting Characteristics of Corrugated Surfaces Based on Single-Factor and Taguchi Methods

Yannian Zhang[1], **Weilong Zhao**[2] and **Haikun Zheng**[3,*]

[1]Pingdingshan Shenma Construction Engineering Group Co., Ltd., Pingdingshan, China
[2]School of Civil Engineering, Henan Polytechnic University, Jiaozuo, China
[3]School of Mechanical and Power Engineering, Henan Polytechnic University, Jiaozuo, China

*Corresponding Author: Haikun Zheng. Email: hkzheng@hpu.edu.cn

Received: 11 April 2026; Accepted: 25 May 2026; Published: 31 August 2026

ABSTRACT: Aiming at the frosting problem of heat exchanger with fins and tubes under low temperature and high humidity conditions, this study combines the single factor method with the Taguchi experimental method. A corrugated surface was used as the experimental object instead of a corrugated fin, and the frosting characteristics of corrugated surfaces with different structural parameters, including corrugation angle, corrugation depth, and corrugation distribution, were investigated. The Taguchi experimental method was further employed to evaluate the frosting performance of the corrugated surfaces. At the same frosting duration, the surface with a corrugated left section and a plain right section showed the greatest frost accumulation and frost layer thickness. The surface with a plain left section and a corrugated right section exhibited the lowest frost accumulation, while the fully corrugated surface exhibited the thinnest frost layer. Compared with corrugation depth and corrugation distribution, corrugation angle had the most significant influence on both frost amount and frost layer thickness, with contribution rates of 57.3% and 44.3%, respectively. Within the range of structural parameters investigated, the optimal parameter combination for minimizing frost amount was A1B1C3, corresponding to a corrugation angle of 11.3°, a corrugation depth of 1 mm, and a surface distribution with a corrugated left section and a plain right section. The optimal combination for minimizing frost layer thickness was A1B1C1, corresponding to a corrugation angle of 11.3°, a corrugation depth of 1 mm, and a fully corrugated distribution. In contrast, the parameter combination resulting in the greatest frost amount and frost layer thickness was A4B3C2, corresponding to a corrugation angle of 42.8°, a corrugation depth of 3 mm, and a surface distribution with a corrugated left half and a flat right half. These results indicate that smaller corrugation angles and corrugation depths help suppress surface frost formation, and an appropriate corrugation distribution can further enhance the surface resistance to frosting. The optimal combinations of structural parameters identified in this study can provide guidance for the future development of corrugated fin structures that combine frost suppression with high heat transfer efficiency.

KEYWORDS: Frosting; corrugated surface; surface structure

1 Introduction

Frost formation on heat exchangers is a common issue in refrigeration and air conditioning systems. Under low-temperature and high-humidity conditions, frost readily accumulates on the fins of widely used heat exchangers with fins and tubes [1,2]. Frost deposition reduces the fin spacing and obstructs airflow, thereby increasing the air-side pressure drop. Consequently, heat transfer performance deteriorates, and in severe cases, the system may fail to operate properly [3–5].

Extensive studies have been conducted to enhance the heat transfer performance of heat exchangers with fins and tubes. To enhance thermal efficiency, various fin geometries have been developed, including slotted, louvered, and corrugated fins. Among them, corrugated fins have shown better overall performance than flat fins [6–8]. Owing to the complex geometry of heat exchangers with fins and tubes and the difficulty of directly observing detailed surface phenomena in experiments, simplified models are often used, in which flat-fin tubes are represented by flat plates and corrugated fins by corrugated plates [9–11], hereafter referred to as corrugated surfaces. Extensive theoretical and experimental studies have examined the heat transfer and pressure drop characteristics of flow channels formed by corrugated surfaces [12–14].

When fluid flows over a corrugated surface, the corrugation geometry can induce vortices, secondary flows, and local impingement flows, thereby enhancing near wall flow disturbance, promoting fluid mixing, and improving convective heat transfer. The intensity of these secondary flow structures is closely associated with the Reynolds number (Re), corrugation angle, corrugation pitch, and waveform geometry. Obaidi et al. systematically investigated the flow and heat transfer characteristics of hot water in corrugated tubes under a constant heat flux using numerical simulations. Their results showed that, although corrugated structures increase pressure drop and frictional resistance, they can significantly enhance the Nusselt number and overall thermal performance [15]. Karabulut and Alnak numerically compared the flow and heat transfer performance of straight channels and channels with semicircular corrugated grooves, and found that an appropriate corrugation angle can effectively enhance heat transfer and improve the overall thermal performance of the channel [16]. Lu et al. further demonstrated that corrugated plate structures can enhance heat transfer by improving the synergy between the velocity and temperature fields and by inducing secondary flows. In particular, a smaller corrugation pitch was found to increase the Nusselt number, while also resulting in a higher pressure drop [17].

Corrugated channels with a V shaped structure have attracted considerable attention in recent years because their sharp bends can induce strong local flow disturbances and secondary flows, thereby enhancing fluid mixing and heat transfer. Abdel-Aziz et al. [18] reported that the sharp edges of corrugated structures, particularly those in V shaped corrugations, play a key role in intensifying flow disturbance and improving heat transfer performance. Yang and Chen [19] performed a detailed numerical investigation of the flow and heat transfer characteristics in V shaped corrugated channels and validated their simulation results, demonstrating the reliability of the numerical model. Parlak [20] investigated the flow characteristics at Reynolds numbers ranging from 100 to 400 and found that, under practical pressure drop constraints, the optimized corrugated channel with a V shaped configuration increased the Nusselt number by 27.3% compared with a straight channel. These findings indicate that V shaped corrugated channels exhibit superior heat transfer performance compared with conventional straight channels [21].

Zhou, Liu, and colleagues [22,23] investigated frosting behavior on corrugated surfaces using numerical and experimental methods, respectively. Their results showed that, under identical operating conditions, the frost layer formed on corrugated surfaces was thinner than that on flat surfaces, suggesting that corrugated structures can suppress frost growth to some extent. In addition to modifying the structural characteristics of corrugated surfaces, some researchers have attempted to improve the overall performance of heat exchangers with fins and tubes by optimizing fin configurations. Tao et al. [24] proposed a novel composite fin structure, in which corrugated fins were arranged on the upstream side and flat fins on the downstream side, and compared its performance with those of fully corrugated and fully flat fin configurations. Their results showed that, under the same Reynolds number, the composite fin structure exhibited the best overall thermal performance. Shi and Hussein et al. [25,26] found that increasing the corrugation angle enhanced the Nusselt number, but also increased the friction factor and pressure drop, which could reduce the overall thermos hydraulic performance. Zhang et al. [27] further reported that the corrugation angle significantly affected the local Nusselt number distribution and fin efficiency. In the same region, the fin efficiency at the inlet of corrugated fins was higher than that of flat fins [28].

In summary, surface structure has a significant impact on the heat transfer characteristics and performance of corrugated surfaces. Previous studies have largely focused on the influence of individual structural factors on frosting behavior; for example, they have examined only the effects of corrugation patterns or variations in corrugation depth on frost layer growth, frost layer thickness, and heat transfer performance, while lacking a systematic analysis of the combined effects of multiple structural parameters on corrugated surfaces. To address these shortcomings, this study takes corrugated surfaces as its subject and comprehensively considers key structural parameters such as corrugation angle, depth, and distribution to systematically investigate the effects of different structural combinations on surface frosting characteristics. Compared to previous research, this study provides a more detailed and comprehensive analysis of the mechanisms by which corrugated surface structural parameters influence the frosting process, offering more valuable experimental evidence for optimizing the surface structure and designing frost suppression measures for finned tube heat exchangers in low-temperature, high-humidity environments.

2 Experimental System and Working Conditions

2.1 Surface Preparation

Fig. 1 illustrates the structural parameters of the experimental aluminum corrugated surface (hereafter referred to as the corrugated surface). The specific geometric parameters of this corrugated surface are provided in Table 1.

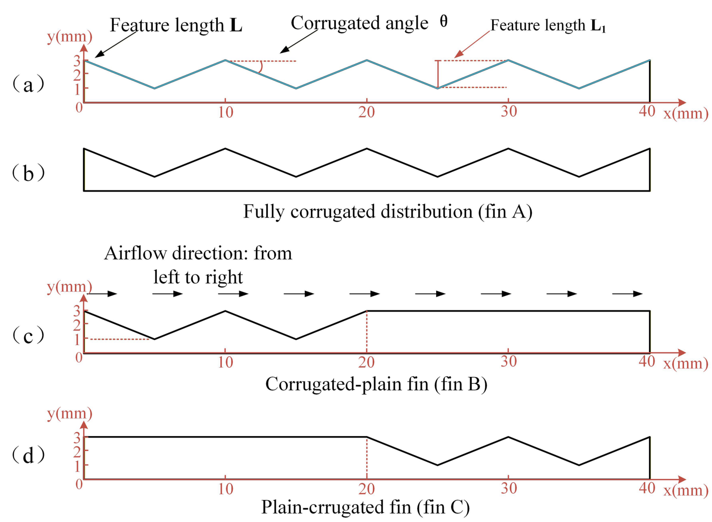

Figure 1: Schematic diagram of structural parameters of corrugated surface. (**a**) Characteristic length, angle, and distribution of the corrugations; (**b**) Fully corrugated surface; (**c**) left-corrugated/right-plain surface; (**d**) left-plain/right-corrugated surface.

Table 1: Structural parameters of corrugated surface for experiment.

Serial Number	Corrugation Angle θ/°	Corrugation depth L_1/mm	Corrugation Distribution
Case 1	11.3	1	Full corrugation
Case 2	21.8	1	Full corrugation
Case 3	32.3	1	Full corrugation
Case 4	42.8	1	Full corrugation
Case 5	11.3	2	Full corrugation
Case 6	11.3	3	Full corrugation
Case 7	11.3	1	Left half corrugated–right half flat
Case 8	11.3	1	Right half corrugated–left half flat
Case 9	--	--	Flat plate

The preparation process for a fully corrugated surface is detailed as follows. The corrugated surface, with dimensions of 40 mm ∗ 40 mm ∗ 3 mm, was cut from pure aluminum (1060 Al) using a wire cut electric discharge machine (Hengshida DK7732). To ensure accurate measurement of the cold surface temperature during the experiments, four blind holes were drilled into the side of the corrugated surface using an electric discharge punch (Aocheng DD703). These holes, each with a diameter of 1 mm and a depth of 10 mm, served as locations for thermocouple placement. The prepared corrugated surface was then immersed in alcohol and subsequently cleaned repeatedly using an ultrasonic cleaner (FUYANG F-009S) to effectively remove any residual surface contaminants. Finally, the surface was dried in a drying oven (LICHEN 202-00s) and stored until use. The dimensional characteristics of the corrugated surface and the arrangement of the thermocouples are presented in Fig. 2.

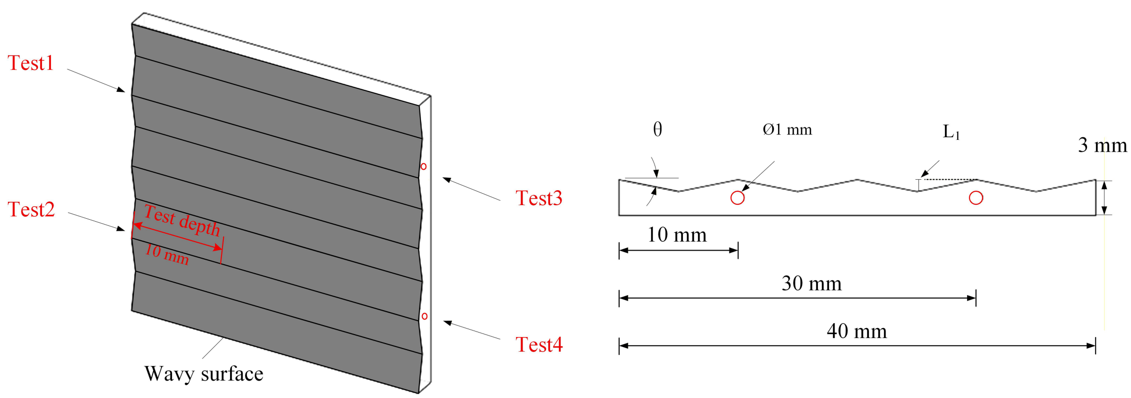

Figure 2: Experimental cold surface dimensional characteristics and thermocouple layout.

It should be noted that this study mainly focused on the effects of macroscopic corrugated surface parameters, including corrugated angle, corrugated depth, and corrugated distribution, on frosting characteristics. Surface roughness and machining accuracy were not treated as independent variables in this study. To reduce the influence of these microscopic surface characteristics on the experimental results, all specimens were prepared using the same material and manufacturing process, and the same cleaning and drying procedures were applied before the experiments. Therefore, the effects of surface roughness and machining accuracy were minimized as much as possible and treated as controlled factors in the present work.

2.2 Experimental Method

Fig. 3 presents a schematic diagram of the visual low-temperature frosting experimental platform, which comprises three main systems: the moist air conditioning system, the low-temperature test bench system, and the data and image acquisition system [29]. Fig. 4 shows the physical setup of the measuring instruments used in the experiment, including the data acquisition unit, CCD camera, and precision electronic balance. The specific experimental procedure is outlined below:

1. Preparation: Before commencing the experiment, the corrugated surface placed on the liquid cooling platform within the low-temperature test bench system is first wrapped with a polymer plastic film. This prevents premature frost formation on the corrugated surface before the target experimental conditions are established.
2. Stabilization: The visual low-temperature frosting experimental platform is initiated, and the operating conditions for the frosting experiment are adjusted until a steady state is achieved.
3. Initiation: The plastic film covering the experimental corrugated surface is removed, and the frosting experiment is immediately started.
4. Measurement: Upon completion of the experiment, the corrugated surface is removed, and its total mass m1, is measured using a precision electronic balance. Subsequently, the frost layer is allowed to dry, and the resulting mass of the surface m2, is measured again. The difference between these two measurements (m1–m2), quantifies the mass of frost accumulated on the experimental cold surface.

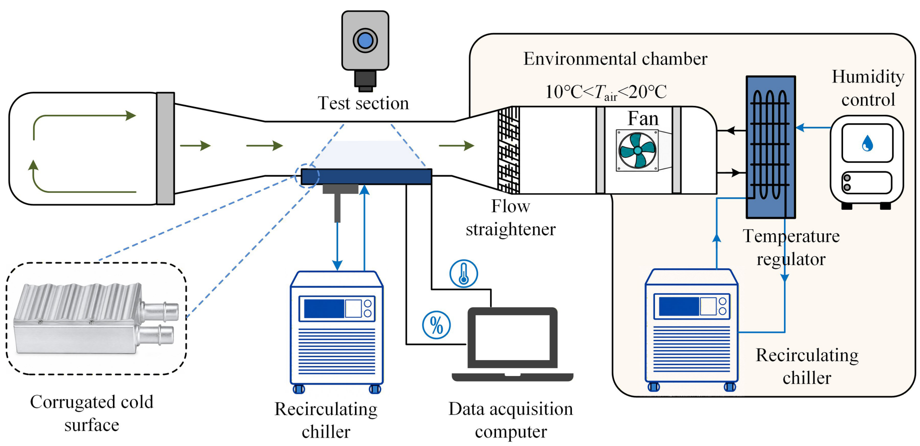

Figure 3: Schematic diagram of visualized low-temperature frosting experiment platform.

(a) Data acquisition instrument (b) Precision electronic balance (c) CCD microcamera

Figure 4: Measuring instruments used in the experiment. (**a**) data acquisition instrument; (**b**) precision electronic balance; and (**c**) CCD microcamera.

The frost layer thickness in this experiment is defined as the vertical distance from the top of the frost layer to the cold surface. The average frost layer thickness, δ, can be calculated using the following Eq. (1):

$$\delta = \frac{\sum_{j=1}^{n} \Delta y_j}{n} \tag{1}$$

During the experiment, the CCD microscope camera integrated within the data and image acquisition system was used to capture side view images of the frost layer forming on the experimental surface. The acquired images were subsequently processed using Image Pro Plus Version software to calculate the average frost layer thickness, δ, which was taken as the experimental value.

2.3 Data Processing

Under the established frosting experimental conditions, the flow of moist air over corrugated surfaces with different structural parameters leads to variations in the convective heat transfer process and overall heat transfer performance. The heat transfer intensity directly affects the growth behavior of the frost layer on the corrugated surface. The Reynolds number for the moist air flowing over the corrugated surface can be calculated using the following equation [30]:

$$Re = \frac{\rho_{air} v L}{\mu} \tag{2}$$

where ρ_{air} is the density of moist air, kg/m^3; v is the velocity of moist air, m/s; L is the characteristic length, which is the length of the corrugation side, mm; and μ is the viscosity, kg/(m·s). In this study, the characteristic length L was defined as the actual flow length along the corrugated surface, namely the corrugation side length or unfolded corrugation length. In this way, the geometric effect of the corrugated structure was incorporated into the calculation of *Re*, *Nu*, and *h*.

The Nusselt number *Nu* of moist air flowing over the corrugated surface can be calculated using the following formula [30]:

$$Nu = 0.664 Re^{1/2} \cdot Pr^{1/3} \tag{3}$$

where *Pr* is the Prandtl number (dimensionless number). The corrugated surface promotes local flow disturbance, vortex generation, and secondary mixing, which may enhance convective heat transfer compared with a smooth flat surface. In the present study, the above correlation was used as an equivalent simplified correlation to evaluate the relative heat transfer tendency among different corrugated structures under identical experimental conditions. The influence of the corrugated geometry was considered through the characteristic length L and the actual heat transfer area A.

Since

$$Nu = \frac{hL}{\lambda} \tag{4}$$

where λ is the thermal conductivity of moist air, W/(m^2·°C); h is the convective heat transfer coefficient, W/(m^2·°C).

The convective heat transfer coefficient h of moist air flowing over the corrugated surface, combined with Eqs. (2)–(4), can be calculated as follows:

$$h = \frac{\lambda Nu}{L} = \frac{\lambda}{L} \cdot 0.664 Re_L^{1/2} \cdot Pr^{1/3} \tag{5}$$

The heat transfer per unit time Q of the corrugated surface can be calculated by the following formula [30]:

$$Q = hA\Delta t = \frac{\lambda}{L}\mathrm{A} \cdot 0.664 \cdot \left(\frac{\rho_{air} v L}{\mu}\right)^{1/2} \cdot Pr^{1/3} \cdot \Delta t \tag{6}$$

In the above content,

$$\Delta t = T_{air} - T_w \tag{7}$$

where A is the surface heat transfer area on the corrugated surface, m^2; "Δt" Heat exchange temperature difference, °C. T_w is the cold surface temperature, °C; T_{air} is the moist air temperature, °C.

Under identical experimental conditions, the thermophysical properties of moist air, inlet velocity, and temperature difference were kept constant. For the simplified heat transfer calculation, the secondary flow disturbance induced near the corrugated surface was neglected, and the geometrical variations among different structures were represented by the corrugation characteristic length L and the actual heat transfer area A. Accordingly, the calculated variations in the Nusselt number (Nu), convective heat transfer coefficient (h), and heat transfer rate (Q) mainly reflect the effects of the varying L and A values.

To assess the reliability of the experimental results, each set of operating conditions was repeated three times under identical conditions. The data presented in Figs. 5–10 represent the average values obtained from the three replicate experiments, and the error bars indicate the expanded uncertainty of the corresponding parameters. Table 2 lists the measurement ranges, accuracies, standard uncertainties, and expanded uncertainties of the main measuring instruments. For the instrument accuracy, denoted by a, and assuming that the measurement error follows a rectangular distribution, the Type B standard uncertainty can be expressed as:

$$u_B = a/\sqrt{3} \tag{8}$$

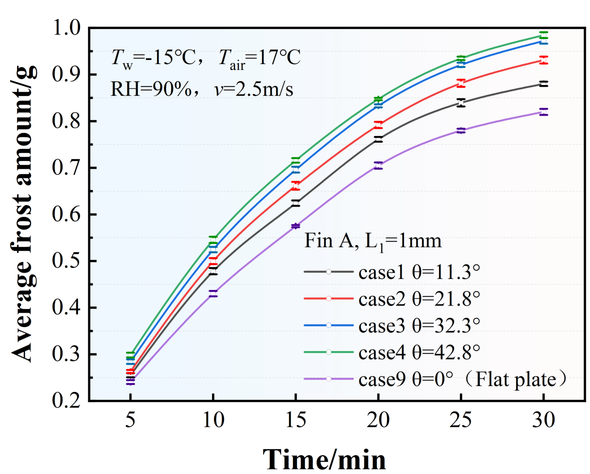

Figure 5: Effect of corrugation angle on frost amount.

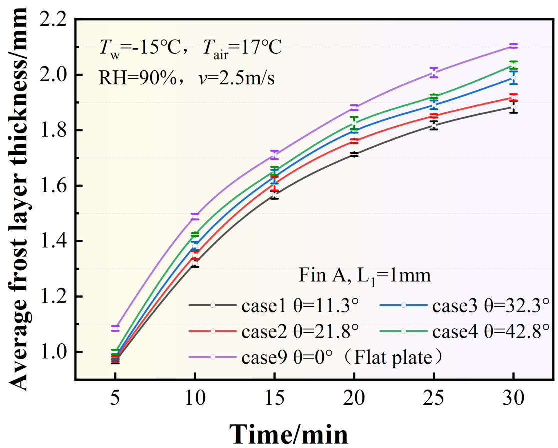

Figure 6: Effect of corrugation angle on frost layer thickness.

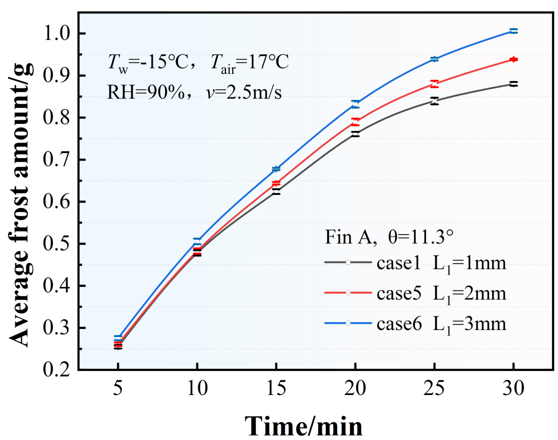

Figure 7: Effect of corrugation depth on frost amount.

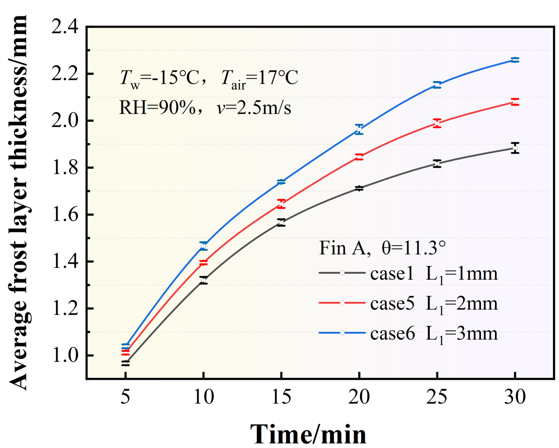

Figure 8: Effect of corrugation depth on frost layer thickness.

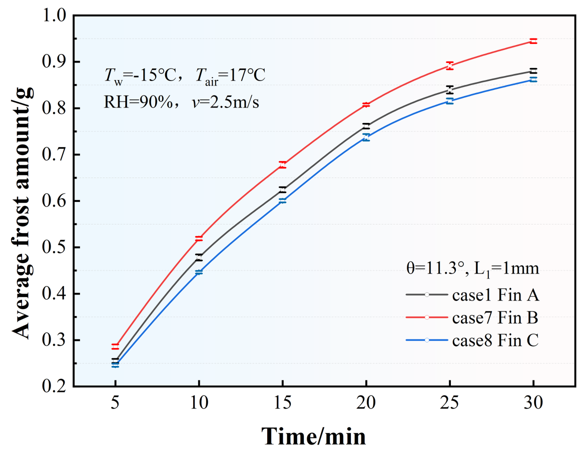

Figure 9: Effect of corrugation distribution on frost amount.

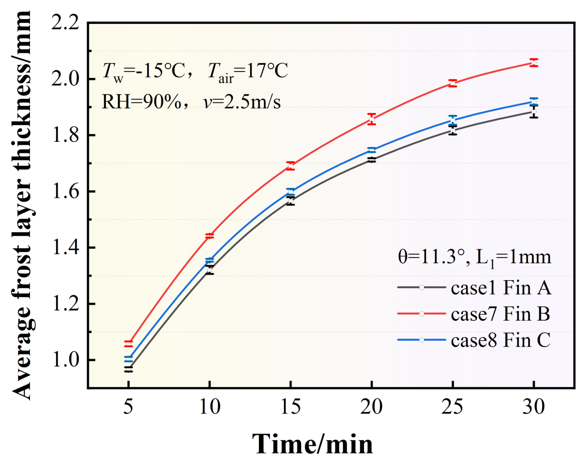

Figure 10: Effect of corrugation distribution on frost layer thickness.

Table 2: Range and accuracy of experimental measuring instruments.

Equipment	Measurement Range	Accuracy	Standard Uncertainty	Expanded Uncertainty
Type T thermocouple	−40°C~105°C	±0.1°C	0.0577°C	±0.115°C
Precision electronic balance	0~200 g	0.0001 g	5.77×10^{-5} g	$\pm 1.15 \times 10^{-4}$ g
Flow meter	10~100 mL/min	±4%	2.31%	±4.62%
Thermal anemometer	0~15 m/s	±0.1 m/s (0–2 m/s) ±0.3 m/s (2–15 m/s)	0.0577 m/s 0.173 m/s	0.115 m/s 0.346 m/s
Temperature sensor	−20°C~80°C	±0.3°C	0.173°C	±0.346°C
Humidity sensor	0%~99%	±2%	1.15%RH	±2.31%RH

The expanded uncertainty was calculated as:

$$U = ku_B \tag{9}$$

The coverage factor was set to $k = 2$, corresponding to a confidence level of approximately 95%. The uncertainties listed in Table 2 primarily represent Type B uncertainties arising from instrument accuracy, whereas the error bars in Figs. 5–10 additionally account for the variability among the three replicate experiments. This approach enables the effects of measurement errors on the experimental results and Taguchi optimization analysis to be evaluated.

3 Analysis of the Influence of Structural Parameters on Frosting Characteristics

The experimental conditions of this paper are: $T_w = -15°C$, $T_{air} = 17°C$, RH = 90%, $v = 2.5$ m/s, The relative humidity of the environment remained constant throughout the experiment. Using the aforementioned formulas and operating under the same experimental conditions, the influence of various structural parameters on the wet air flow over the corrugated surface and the related heat transfer parameters (*Nu, h, Q*) was calculated. The specific calculated values are presented in Table 3.

Table 3: Effects of structural parameters on *Nu*, *h* and *Q* under the same experimental conditions.

Serial Number	θ/°	L_1/mm	Corrugation Distribution	L/mm	$A/10^{-3}$ m^2	Nu	$h/(W\cdot m^{-2}\cdot K^{-1})$	Q/W
Case1	11.3	1	Full corrugation	40.7922	1.63	51.74	30.57	1.596
Case2	21.8	1	Full corrugation	43.0812	1.72	53.18	29.75	1.640
Case3	32.3	1	Full corrugation	47.3221	1.89	55.73	28.38	1.719
Case4	42.8	1	Full corrugation	54.4592	2.18	59.79	26.46	1.844
Case5	11.3	2	Full corrugation	40.7922	1.63	51.74	30.57	1.596
Case6	11.3	3	Full Corrugation	40.7907	1.63	51.74	30.57	1.596
Case7	11.3	1	Left half corrugated–right half flat	40.3961	1.62	51.49	30.72	1.588
Case8	11.3	1	Right half corrugated–left half flat	40.3961	1.62	51.49	30.72	1.588
Case9	–	–	Flat plate	40	1.60	51.24	30.87	1.581

3.1 Effect of Corrugation Angle on Frosting Characteristics

As demonstrated in Fig. 5, under the same frosting conditions, the mass of the frost layer accumulated on corrugated surfaces increases with the increase in the corrugation angle, and the mass of the frost layer on all corrugated surfaces is higher than that on flat surfaces. This phenomenon can be attributed to the synergistic enhancement of heat and mass transfer processes by the corrugated structure. According to Eq. (6) and Table 3, as the corrugation angle increases, the surface characteristic length, Nusselt number, and effective heat transfer area all increase, thereby enhancing the overall heat transfer capacity between the moist air and the low-temperature wall surface. This enhanced heat transfer process facilitates the release of latent heat and the deposition of water vapor from the air onto the cold surface through condensation.

In addition, a larger corrugation angle intensifies geometric disturbances within the flow channel, making the airflow more prone to deflection, local deceleration, and separation near the corrugated wall. These local flow disturbances modify the near wall velocity and concentration boundary layers, thereby promoting the diffusion and transport of water vapor toward the colder surface. Consequently, under the same frosting duration, Case 4, which had the largest corrugation angle, exhibited the highest frost layer mass, followed by Cases 3, 2, and 1, whereas the flat surface, Case 9, showed the lowest frost layer mass. It can also be observed that, as the frost layer continued to thicken, its thermal resistance gradually increased, resulting in a reduced frosting rate on all surfaces during the later stages.

Fig. 5 reveals that as the corrugation angle increases to a certain extent, the frost mass in Case 3 gradually approaches that of Case 4, particularly during the middle and late stages of frosting (15 to 30 min). This phenomenon occurs because a larger corrugation angle, while initially promoting more frost, also leads to a more pronounced decrease in the characteristic length (L') of the surface frost layer and a more significant increase in the thermal resistance of the growing frost layer. In the middle and late stages, as the frost layer progressively fills the surface grooves, the overall heat transfer capacity of the corrugated surface is diminished. This reduction is more significant for the surface with the largest corrugation angle (Case 4), causing the rate of frost growth in Case 3 to nearly converge with that of Case 4.

Quantitatively, after 30 min of frosting, the frost mass increase relative to the flat surface (Case 9) was 7.34%, 13.54%, 18.54%, and 20.04% for Case 1, Case 2, Case 3, and Case 4, respectively.

As depicted in Fig. 6, for a consistent frosting duration, the frost layer thickness on the corrugated surface increases with a larger corrugation angle. Consequently, the corrugated surface in Case 4 exhibits the thickest frost layer, followed sequentially by Case 3, Case 2, and Case 1. This trend is directly correlated with the previously established finding: a larger corrugation angle promotes a greater mass of frost amount on the surface, which inevitably translates to an increased frost layer thickness.

However, a key observation from Fig. 6 is that the frost layer thickness on the corrugated surfaces is smaller than that on the flat surface (Case 9). Although the mass of frost on the flat surface is lower than on the corrugated surfaces, the characteristic length (L) of the flat surface is significantly smaller. Because the frost layer thickness is inversely proportional to the surface characteristic length (when frost mass is constant), the rate of thickness increase on the flat surface is higher than that on the corrugated surfaces, resulting in a generally thinner layer on the patterned surfaces.

Close examination of Fig. 6 reveals a change in the growth rate during the late frosting period (25 to 30 min). Specifically, the frost layer thickness growth rate in Case 1 and Case 2 gradually decreases, while it gradually increases in Case 3 and Case 4. This behavior is related to the groove filling process. For surfaces with larger corrugation angles (Cases 3 and 4), the greater mass of accumulated frost facilitates the faster filling of the grooves by the growing frost layer. This process leads to a sharper reduction in the characteristic length ($L^{'}$) of the developing frost layer on the corrugated surface. The reduction in the effective characteristic length, in turn, contributes to an accelerated increase in the frost layer thickness growth rate, explaining why the rates in Case 3 and Case 4 become more pronounced than those in Case 1 and Case 2 in the late stage. Furthermore, the growth rate in Case 4 exceeds that in Case 3.

Quantitatively, after 30 min of frosting, the average frost layer thicknesses in Cases 2, 3, 4, and 9 increased by 1.83%, 5.57%, 8.01%, and 11.66%, respectively, compared with that in Case 1. It should be noted that the 1.83% increase in Case 2 was relatively small and of the same order of magnitude as the uncertainty range; therefore, this difference is interpreted only as a slight upward trend. In contrast, the larger increases observed in Cases 3, 4, and 9 were more clearly distinguishable from the uncertainty range, indicating that the observed increase in frost layer thickness is highly reliable.

3.2 Effect of Corrugation Depth on Frosting Characteristics

Figs. 7 and 8 clearly demonstrate that, over a constant frosting duration, both the mass of accumulated frost and the frost layer thickness on the corrugated surface increase with greater corrugation depth. This trend is explained by the influence of depth on the groove filling dynamics during the frosting process. Although the pre-frosting heat transfer rate per unit time for the corrugated surfaces is consistent with the values listed in Table 3, the actual heat transfer during frosting differs. For deeper corrugated structures, the growing frost layer cannot completely fill the surface grooves within a short period. Consequently, the effective feature length of the corrugated surface decreases more slowly after frosting, enabling it to maintain a relatively high heat transfer capacity over an extended frosting period. This promotes the continuous sublimation deposition of water vapor, ultimately resulting in greater frost mass and a thicker frost layer.

In addition to heat transfer effects, increased corrugation depth significantly alters the local flow and mass transfer characteristics within the channels. Deeper corrugation grooves enhance the geometric nonuniformity of the flow path, resulting in more pronounced velocity gradients and recirculation zones near the peaks, troughs, and groove regions. Although these low velocity zones reduce the local air renewal rate, they prolong the residence time of moist air near the low-temperature wall, thereby facilitating water vapor diffusion and frost crystal nucleation. Therefore, the increase in frost formation associated with greater corrugation depth cannot be attributed solely to changes in characteristic length or heat transfer area. Instead, it results from the combined effects of delayed groove filling, prolonged water vapor residence, enhanced diffusion, an expanded effective nucleation area, and localized channel blockage. Together, these mechanisms strengthen the geometrically induced coupling between heat and mass transfer, enabling more water vapor to deposit on deeper corrugated surfaces.

Focusing on Fig. 8, the frost layer thickness in Cases 5 and 6 is markedly greater than that in Case 1 for the same frosting time, a difference that becomes particularly significant during the middle and later stages of frosting (15 to 30 min). Since Cases 5 and 6 have deeper corrugations than Case 1, the grooves are more resistant to being filled by the growing frost layer. This resistance ensures that the characteristic length (L') of the frost layer remains higher in Cases 5 and 6 compared to Case 1. The maintained larger L' results in sustained higher heat transfer, leading to a greater frost mass and a thicker layer. In contrast, the shallower corrugations of Case 1 are filled much earlier in the process. Once filled, the surface effectively becomes flat, leading to a significant reduction in the heat transfer capacity and a corresponding slowdown in the growth rates of both frost mass and thickness. This difference in filling time is why the frost layer thickness in Cases 5 and 6 becomes substantially greater than that in Case 1 during the later stages.

Quantitatively, after 30 min of frosting, the frost mass in Case 5 and Case 6 increased by 6.61% and 14.31%, respectively, compared to Case 1. Correspondingly, the frost layer thickness in Case 5 and Case 6 increased by 10.41% and 19.92%, respectively, relative to Case 1.

3.3 Effect of Corrugation Distribution on Frosting Characteristics

As shown in Fig. 9, under identical frosting durations, the surface frost amount follows the order: Case 7 (left half corrugated–right half flat) > Case 1 (fully corrugated) > Case 8 (right half corrugated–left half flat). This trend can be explained by the heat transfer characteristics of the corrugated surface. Since the moist air flows from left to right, the inlet side air has higher temperature and moisture content, resulting in a higher water vapor partial pressure and a greater driving force for condensation and deposition. Therefore, the left half of the surface plays a dominant role in the overall frosting process. When the left half contains a corrugated structure, as in Cases 7 and 1, the corrugated geometry enhances local airflow turbulence and disrupts the near wall velocity and concentration boundary layers. This promotes more effective contact between the moist air and the cold surface, thereby facilitating water vapor diffusion toward the cold surface, as well as frost crystal nucleation and deposition. Consequently, the amount of frost formed on the left half follows the order Case 7 (left) ≈ Case 1 (left) > Case 8 (left). In contrast, the left half of Case 8 is flat, which weakens airflow turbulence. As a result, the enhanced heat and mass transfer potential of the high-humidity inlet air is not fully utilized, leading to a weaker initial frosting advantage.

As the airflow continues toward the right half, part of the water vapor has already deposited on the cold upstream surface, leading to decreases in air temperature and humidity. Consequently, the local water vapor partial pressure, supersaturation, and driving force for vapor deposition are all reduced. Therefore, frosting in the downstream region is more likely to be limited by insufficient water vapor supply and increased flow resistance. In Cases 1 and 8, the right halves contain corrugated structures. Although these corrugations can still enhance local turbulence, their reinforcing effect under downstream low-humidity conditions is constrained by the combined effects of substantial flow resistance, insufficient air renewal, and increased thermal resistance caused by frost layer growth. In contrast, the right half of Case 7 is flat and has lower flow resistance, making it less prone to local stagnation and blockage. This helps maintain relatively stable air renewal and subsequent heat and mass transfer. Consequently, the amount of frost formed on the right half follows the order Case 7 (right) > Case 1 (right) ≈ Case 8 (right).

Overall, Case 7 simultaneously leverages the enhanced heat and mass transfer induced by the upstream corrugated structure under high-humidity inlet conditions and the lower flow resistance and weaker clogging tendency of the downstream flat structure. This configuration creates a more favorable balance among heat transfer, mass transfer, and flow resistance, ultimately resulting in the highest total frost accumulation. Although Case 1 contains a fully corrugated structure, its downstream corrugated region is constrained by water vapor consumption along the flow path and increased flow resistance. By contrast, because Case 8 has a flat upstream surface, it fails to effectively enhance frosting in the region with the most abundant water vapor supply, resulting in the lowest total frost volume.

As shown in Fig. 10, the same order applies to the frost layer thickness: Case 7 > Case 8 > Case 1. Specifically, the surface in Case 7 exhibited the thickest frost layer, followed by Case 8, while Case 1 showed the thinnest. This behavior arises because, for a given frost mass, a smaller effective heat exchange area results in a thicker frost layer; conversely, for the same surface area, a greater frost mass yields a thicker layer. In Fig. 9, the frost mass ranking is Case 7 > Case 1 > Case 8, with Case 7 showing a substantially higher frost mass than Case 8. Since Cases 7 and 8 have identical heat exchange surface areas, the significantly greater frost mass in Case 7 leads to a correspondingly thicker frost layer. Although the frost mass in Case 1 exceeds that in Case 8, the larger heat exchange area of Case 1 results in a thinner frost layer, making the two cases comparable.

In summary, within the same frosting duration, the frost layer thickness follows the order:

Case 7 > Case 8 > Case 1

that is, left half corrugated–right half flat > right half corrugated–left half flat > fully corrugated.

After 30 min of frosting, compared with Case 8, the frost amount in Cases 1 and 7 increased by 2.15% and 9.61%, respectively. Relative to Case 1, the frost layer thickness in Cases 8 and 7 increased by 1.90% and 9.24%, respectively.

4 Analysis of the Importance of Structural Parameters to Frosting Characteristics

Taguchi experimental method, as a parameter optimization design method commonly used in practical engineering, can study a large number of process variables with the help of orthogonal tables and signal to noise ratio analysis through only a small number of experiments [31]. Based on Taguchi's design of experiments methodology, and considering the long duration of the frosting experiments and the stringent stability requirements of the experimental system, this study established a mixed fractional factorial design matrix comprising eight experimental groups. This matrix was used to preliminarily evaluate the effects of corrugation angle, corrugation depth, and corrugation distribution pattern on frosting performance. It should be noted that the three structural parameters investigated in this study include four, three, and three levels, respectively. The experimental matrix is not a standard L8 or L9 orthogonal array and cannot fully account for factor interactions. Consequently, the results obtained from this experimental matrix are primarily used to identify the relative main effects of each structural parameter on frosting characteristics and to screen potential optimal structural combinations. They are not intended to provide a complete analysis of variance (ANOVA) that includes interaction effects and statistical significance testing. The experimental design and test results are presented in Table 4. Based on the experimental data in Table 4, the signal to noise ratios for each experiment are listed in Table 5.

Table 4: Orthogonal design of surface structure and experimental results.

Experiment	Factor			Result			
	A	B	C	Frost Amount m1/g	Frost Amount m2/g	Frost Layer Thickness δ1/mm	Frost Layer Thickness δ2/mm
1	1	1	1	0.6321	0.6481	1.5218	1.5202
2	2	2	1	0.6710	0.6643	1.6667	1.6687
3	3	3	1	0.7992	0.7906	1.9576	1.9586
4	4	3	2	0.8051	0.8071	2.0734	2.0783
5	4	2	3	0.7360	0.7377	1.8512	1.8587
6	3	1	3	0.7202	0.7230	1.7013	1.7096
7	2	1	2	0.7127	0.7158	1.7666	1.7592
8	1	3	3	0.6124	0.6104	1.6933	1.7002

Table 5: S/N ratio of frost weight and thickness.

Experiment	Factor			Result	
	A	B	C	Frost Amount Signal-to-Noise Ratio S/N	Frost Layer Thickness Signal-to-Noise Ratio S/N
1	1	1	1	3.8744	−3.6425
2	2	2	1	3.5089	−4.4422
3	3	3	1	1.9936	−5.8366
4	4	3	2	1.8722	−6.3441
5	4	2	3	2.6524	−5.3665
6	3	1	3	2.8341	−4.6369
7	2	1	2	2.9230	−4.9246
8	1	3	3	4.2735	−4.5923

This paper adopts the small sight characteristic of the Taguchi experimental method. The smaller the experimental values of frost amount and frost layer thickness, the larger the calculated signal to noise ratio. The signal to noise ratio S/N of frost amount and frost layer thickness can be calculated by the following formula [32]:

$$S/N = -10 \log \Sigma y_i^2 / n \tag{10}$$

In the formula, y_i is the response result of each sample in each experiment, and n is the number of sample iterations.

4.1 Taguchi Experimental Design

Based on the experimental frost amount and frost layer thickness data reported in Table 4, the signal to noise ratio (S/N) for frost mass and frost layer thickness in each trial was computed using Eq. (10); the results are presented in Table 5. Tables 6 and 7 summarize the mean S/N and the contribution rates for each parameter level for frost mass and frost-layer thickness, respectively. The mean S/N value for a given factor level in Tables 6 and 7 is the arithmetic average of the S/N values for that level obtained from Tables 4 and 5. The range *R* for a factor is defined as the difference between its maximum and minimum mean S/N values across levels. The contribution rate of each factor quantifies its relative influence on the measured frosting responses (frost mass and frost layer thickness). Specifically, the contribution rate for a given factor is calculated as the ratio of its range *R* to the sum of the ranges of all factors, expressed as a percentage. Notably, the current Taguchi analysis is based primarily on the assumption of main effects. For the eight experimental groups included in this study, the total degree of freedom was 7. The degrees of freedom for corrugation angle, corrugation depth, and corrugation distribution were 3, 2, and 2, respectively. Accordingly, the current design has no remaining degrees of freedom for independently estimating experimental error or factor interactions. The contribution rates obtained in this study therefore reflect the relative contributions of the main effects, as determined by range analysis of the signal to noise (S/N) ratios.

Table 6: Analysis of S/N ratio and contribution rate of frost amount at each parameter level.

Factor	Frost Amount Signal-to-Noise Ratio S/N				Extremely Poor R	Contribution Rate (%)
	Level 1	Level 2	Level 3	Level 4		
Corrugation angle	4.0739	3.2159	2.4138	2.2623	1.8116	57.3%
Corrugation depth	3.2105	3.0807	2.7131	–	0.4974	15.7%
Corrugation distribution	3.1256	2.3976	3.2533	–	0.8557	27.0%

Table 7: Analysis of S/N ratio and contribution rate of frost layer thickness at each parameter level.

Factor	Frost Layer Thickness Signal-to-Noise Ratio S/N				Extremely Poor R	Contribution Rate (%)
	Level 1	Level 2	Level 3	Level 4		
Corrugation angle	−4.1174	−4.6834	−5.2367	−5.8553	1.7379	44.3%
Corrugation depth	−4.4013	−4.9044	−5.5910	–	1.1897	30.3%
Corrugation distribution	−4.6405	−5.6343	−4.8652	–	0.9939	25.4%

4.2 Analysis of Taguchi Experimental Results

Based on the calculation results in Tables 6 and 7, the contribution rates of each factor to frost mass were as follows: corrugation angle, 57.3%; corrugation depth, 15.7%; and corrugation distribution, 27.0%. The corresponding contribution rates to frost layer thickness were 44.3%, 30.3%, and 25.4%, respectively. The contribution rates of these factors to frost mass and frost layer thickness are shown in Figs. 11 and 12.

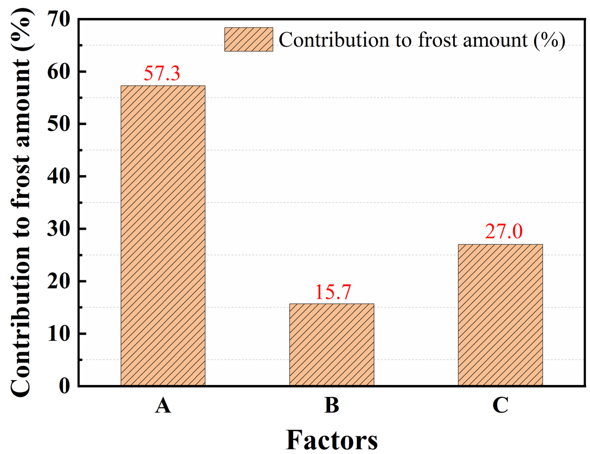

Figure 11: Contribution rate of each factor to frost amount.

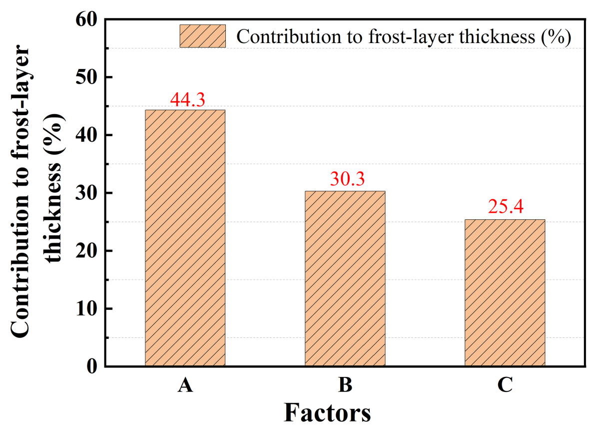

Figure 12: Contribution rate of each factor to frost layer thickness.

Because the signal to noise ratio in the Taguchi analysis was calculated from the experimental response values, the measurement uncertainties in frost amount and frost layer thickness were propagated to the corresponding signal to noise ratios, potentially affecting the evaluation of factor contributions and the determination of optimal levels. Therefore, this study assessed the reliability of the Taguchi analysis results based on the outcomes of three replicate experiments and their corresponding error ranges. The results indicate that, after accounting for experimental uncertainties, the ranking of the primary influencing factors remained largely unchanged. For frost amount, the order of factor importance was corrugation angle > corrugation distribution > corrugation depth. For frost layer thickness, the order was corrugation angle > corrugation depth > corrugation distribution. These results demonstrate that corrugation angle remained the dominant factor affecting both frost mass and frost layer thickness, indicating that the Taguchi optimization results obtained in this study exhibited good stability within the range of experimental uncertainty.

It should be noted that, for factors with low contribution rates or only small variations in the signal to noise ratio across different levels, their effects may be of the same order of magnitude as the experimental uncertainty. Therefore, these effects should be interpreted as trends rather than overinterpreted as having a significant impact. In contrast, corrugation angle exhibits both a large variation in the signal to noise ratio and a high relative contribution rate, indicating that its dominant role is highly reliable.

Figs. 13 and 14 illustrate the signal to noise ratio (S/N) for each level of the investigated factors, which is used to identify the optimal combination of structural parameters that minimizes both the frost mass and the frost layer thickness under the tested operating conditions. Since the Taguchi experimental design in this study follows the "smaller the better" criterion, a higher S/N ratio for a given factor level indicates a stronger influence on the response and a lower corresponding frost mass and frost layer thickness.

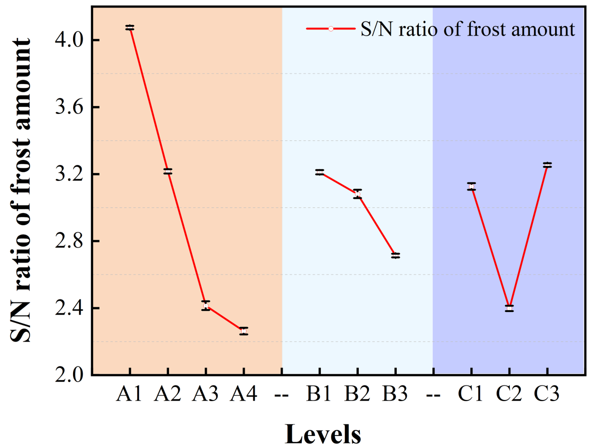

Figure 13: S/N ratio of frost amount at each factor level.

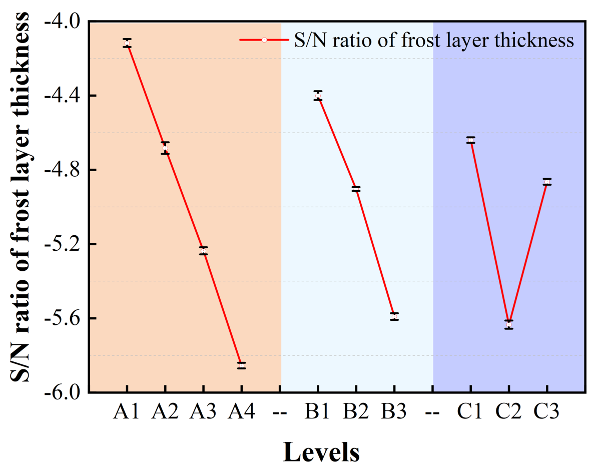

Figure 14: S/N ratio of frost layer thickness for each factor level.

As shown in Figs. 13 and 14 the main effect analysis of the S/N ratios indicates that A1B1C3 is the candidate favorable structural parameter combination for reducing frost amount, corresponding to a corrugation angle of 11.3°, a corrugation depth of 1 mm, and a right half corrugation distribution. For frost layer thickness, A1B1C1 is identified as the candidate favorable combination under the present main effect model, corresponding to a corrugation angle of 11.3°, a corrugation depth of 1 mm, and a fully corrugated distribution.

Experimental verification was conducted for both combinations (A1B1C3 and A1B1C1). The results show that, under identical operating conditions, the frost amount in the A1B1C3 validation experiment decreased to 0.5613 g. Compared with the minimum frost mass of 0.6104 g reported in Table 4, this corresponds to a reduction of approximately 8.04%. These findings indicate that, under the experimental conditions described in this study, this structural combination exhibits a certain degree of frost suppression potential. In contrast, the frost layer thickness in the A1B1C1 validation experiment was 1.5196 mm, which is only 0.0006 mm lower than the minimum value of 1.5202 mm reported in Table 4, corresponding to a relative reduction of approximately 0.039%. Therefore, the improvement in frost layer thickness is negligible, and its statistical significance and engineering relevance require further verification through additional repeated experiments. On this basis, A1B1C1 is considered a candidate structure under the current main effect model, rather than a globally optimal structure in a strict statistical sense.

Further analysis of Figs. 13 and 14 indicates that the structural parameter combination with the lowest S/N ratio, i.e., the combination associated with the maximum frost mass and frost layer thickness, is A4B3C2. Experimental verification showed that, under the same conditions, A4B3C2 produced a frost mass of 0.8081 g and a frost layer thickness of 2.0791 mm. Both values were higher than the maximum values reported in Table 4, which were 0.8071 g and 2.0783 mm, respectively. This confirms the consistency between the experimental results and the Taguchi analysis.

The higher frost mass and frost layer thickness observed for A4B3C2 indicate an enhanced heat transfer capacity of the corrugated surface under these conditions.

In summary, the three structural parameter combinations identified above, namely A1B1C3, A1B1C1, and A4B3C2, provide important guidance for the design and optimization of corrugated surfaces that combine frost suppression with high heat transfer efficiency.

5 Conclusion

In this study, the influence of key surface structural parameters, namely corrugation angle, corrugation depth, and corrugation distribution, on the frosting characteristics of corrugated surfaces was experimentally examined under a fixed and well controlled operating condition: wall temperature T_w = −15°C, air temperature T_{air} = 17°C, relative humidity RH = 90%, and air velocity v = 2.5 m/s. The effects of these parameters on frost amount accumulation and frost layer growth were systematically quantified, and the relative importance of each structural parameter was assessed. Based on the comparative results obtained under the present testing condition, the main conclusions are summarized as follows:

(1) Effect of corrugation angle: As the corrugation angle increases, both the surface frost mass and frost layer thickness increase. However, when the corrugation angle exceeds a certain threshold, its influence on the frost mass gradually weakens. Under the same frosting duration, the frost mass on the corrugated surface is greater than that on a flat surface, whereas the frost layer thickness is smaller than that on the flat surface.

(2) Effect of corrugation depth: Under identical frosting conditions, increasing the corrugation depth leads to higher surface frost mass and greater frost layer thickness. After 30 min of frosting, compared with a corrugation depth of 1 mm, surfaces with corrugation depths of 2 and 3 mm exhibited increases in frost mass by 6.61% and 14.31%, and in frost layer thickness by 10.41% and 19.92%, respectively.

(3) Effect of corrugation distribution: At the same frosting time, the surface with a left-half corrugation–right-half flat plate distribution exhibited the largest frost mass and frost layer thickness, while the right-half corrugation–left-half flat plate distribution showed the smallest frost mass. The full corrugation distribution yielded the smallest frost layer thickness.

(4) Relative importance of structural parameters and optimal combinations: Among the three factors, the corrugation angle exerts the most significant influence on both surface frost mass and frost layer thickness, with contribution rates of 57.3% and 44.3%, respectively. Within the experimental parameter

range, the optimal structural parameter combinations corresponding to the minimum surface frost mass and minimum frost layer thickness are A1B1C3 (corrugation angle 11.3°, depth 1 mm, right-half corrugation distribution) and A1B1C1 (corrugation angle 11.3°, depth 1 mm, full corrugation distribution), respectively. Conversely, the parameter combination A4B3C2 (largest angle, greatest depth, midlevel distribution) results in the maximum frost mass and frost layer thickness.

In summary, the optimized structural parameter combinations identified in this study offer useful insights for the future design of corrugated surfaces with simultaneous frost suppression and heat transfer enhancement. However, since the present conclusions were derived under a fixed operating condition, further investigations over broader ranges of wall temperature, air temperature, relative humidity, and airflow velocity are needed to verify the generality and robustness of the observed trends.

Acknowledgement: Not applicable.

Funding Statement: This work was financially supported by the Science and Technology Research Project of Henan Province (No. 232102241014), the Key Scientific Research Project of Henan Province Colleges and Universities (No. 22A470002) and Doctoral Fund Project of Henan Polytechnic University (No. B2021-37).

Author Contributions: Yannian Zhang: Writing—original draft, Writing—review & editing, Data curation, Validation, Formal analysis. Weilong Zhao: Methodology, Supervision. Haikun Zheng: Data curation, Methodology, Resources, Funding acquisition. All authors reviewed and approved the final version of the manuscript.

Availability of Data and Materials: The authors confirm that the data supporting the findings of this study are available within the article and from the corresponding author upon reasonable request.

Ethics Approval: Not applicable.

Conflicts of Interest: The authors declare no conflicts of interest.

References

1. Chu F, Wu X, Wang L. Meltwater evolution during defrosting on superhydrophobic surfaces. ACS Appl Mater Interfaces. 2018;10(1):1415–21. doi:10.1021/acsami.7b16087.
2. Wang F, Liang C, Zhang X. Research of anti-frosting technology in refrigeration and air conditioning fields: a review. Renew Sustain Energy Rev. 2018;81(2):707–22. doi:10.1016/j.rser.2017.08.046.
3. Han Z, Liu H, Wang Z, Han B, Chang H. Analysis of the long-term growth process of frost layer on the cold surfaces of microchannel heat exchangers. Int J Heat Mass Transf. 2025;247(1–2):127185. doi:10.1016/j.ijheatmasstransfer.2025.127185.
4. Azam MW, Sajjad U, Maqbool F, Sempirini G. Enhancing heat exchanger performance through passive techniques: a comprehensive review. Front Heat Mass Transf. 2026;24(1):2. doi:10.32604/fhmt.2025.074690.
5. Li F, Shi K, Sun X, Yue B, Huang D, Zhao R, et al. Performance evaluation of a vertical-finned microchannel and a fin-tube heat exchangers under wet and frosting conditions. Int J Refrig. 2024;162:158–68. doi:10.1016/j.ijrefrig.2024.03.011.
6. Chang X, Wu X, He A, Chen L, Ding F, Song K. Flow and heat transfer characteristics of a novel m-shaped corrugated fin-and-tube heat exchanger with curved vortex generators. Int Commun Heat Mass Transf. 2026;172(11):110567. doi:10.1016/j.icheatmasstransfer.2026.110567.
7. Abdullah BN, Mohammed KH, Soheel AH, Ali BM, Alomar OR. Analysis of heat transfer inside rectangular micro-channel with wavy surface and hybrid nanofluids. Front Heat Mass Transf. 2025;23(5):1681–700. doi:10.32604/fhmt.2025.066814.

8. Wang Z, Wang R, Li Z, Wang M, Wan L. Numerical investigation on the effect of cylindrical turbulator on performance of corrugated plate-fin heat exchanger. Appl Therm Eng. 2023;230(4):120726. doi:10.1016/j.applthermaleng.2023.120726.
9. Sheng W, Liu P, Dang C, Liu G. Review of restraint frost method on cold surface. Renew Sustain Energy Rev. 2017;79(7):806–13. doi:10.1016/j.rser.2017.05.088.
10. Sheng W, Lan QY, Liu PP, Liu XL, Ding GL. Experimental research and CFD simulation of frosting on aluminum surface. Fluid Mach. 2019;47:83–8,63. (In Chinese).
11. Sheng W, Pei Y, Li X, Ming P, Zhao W. Effect of surface characteristics on condensate droplets growth. Appl Therm Eng. 2020;173(8):115260. doi:10.1016/j.applthermaleng.2020.115260.
12. Jedsadaratanachai W, Boonloi A. 3D numerical analysis on mechanisms of flow and heat transfer in a square channel with right triangular wavy surfaces. Thermophys Aeromech. 2018;25(3):387–404. doi:10.1134/S0869864318030071.
13. Ajeel RK, Salim WSI, Sopian K, Yusoff MZ, Hasnan K, Ibrahim A, et al. Turbulent convective heat transfer of silica oxide nanofluid through corrugated channels: an experimental and numerical study. Int J Heat Mass Transf. 2019;145(133):118806. doi:10.1016/j.ijheatmasstransfer.2019.118806.
14. Kurtulmuş N, Sahin B. A review of hydrodynamics and heat transfer through corrugated channels. Int Commun Heat Mass Transf. 2019;108(17):104307. doi:10.1016/j.icheatmasstransfer.2019.104307.
15. Al-Obaidi AR. Dynamics simulation in corrugated pipe-based investigations of internal thermo-hydraulic flow and improvement of heat performance under various corrugated geometrical configurations. J Therm Anal Calorim. 2024;149(17):9663–88. doi:10.1007/s10973-024-13467-z.
16. Karabulut K, Alnak Y. The influences of various fin and corrugation arrangements on flow characteristics and transfer of heat in ducts of semi-circular grooved using diamond-water nanofluid. J Eng Thermophys. 2025;34(4):857–81. doi:10.1134/S1810232825700341.
17. Lu P, Yang Q, Wei J, Wang S, Huang H. Flow and heat transfer characteristics and field synergy analysis on the corrugated plate with pitches. J Therm Sci Eng Appl. 2023;15(3):031009. doi:10.1115/1.4056385.
18. Abdel-Aziz MH, Hassan I, Nirdosh I, Sedahmed GH. Liquid-solid mass transfer behavior of V-corrugated surfaces under two phase flow. Chem Eng Process Process Intensif. 2013;70:9–16. doi:10.1016/j.cep.2013.05.014.
19. Yang YT, Chen PJ. Numerical simulation of fluid flow and heat transfer characteristics in channel with V corrugated plates. Heat Mass Transf. 2010;46(4):437–45. doi:10.1007/s00231-010-0586-6.
20. Parlak Z. Optimal design of wavy microchannel and comparison of heat transfer characteristics with zigzag and straight geometries. Heat Mass Transf. 2018;54(11):3317–28. doi:10.1007/s00231-018-2375-6.
21. Mehta SK, Pati S. Analysis of thermo-hydraulic performance and entropy generation characteristics for laminar flow through triangular corrugated channel. J Therm Anal Calorim. 2019;136(1):49–62. doi:10.1007/s10973-018-7969-1.
22. Zhou ZY, Ye WL, Zhang RH, Huang HY, Qiu CW, Chen CF. Simulation of the frosting process in corrugated fin heat exchangers. Cryog Supercond. 2024;52:79–85+92. (In Chinese). doi:10.16711/j.1001-7100.2024.08.011.
23. Liu Y, Sheng W, Fang YQ, Zhang PC, Zheng HK, Hao XR. Experimental study on frost formation on aluminum-based corrugated surfaces. J Refrig. 2022;43:78–86. (In Chinese). doi:10.3969/j.issn.0253-4339.2022.03.078.
24. Tao YB, He YL, Wu ZG, Tao WQ. Numerical design of an efficient wavy fin surface based on the local heat transfer coefficient study. J Enh Heat Transf. 2007;14(4):315–32. doi:10.1615/jenhheattransf.v14.i4.50.
25. Shi D. Characterizing, correlating, and evaluating swirl flow and heat transfer in wavy plate-fin channels with novel enhancement attributes [dissertation]. Cincinnati, OH, USA: University of Cincinnati; 2020.
26. Hussein HAM, Zulkifli R, Bin Wan Mahmood WMF, Ajeel RK. Effects of design parameters on flow fields and heat transfer characteristics in semicircle oblique-finned corrugated. Int Commun Heat Mass Transf. 2022;135(2):106143. doi:10.1016/j.icheatmasstransfer.2022.106143.
27. Zhang K, Li MJ, Liu H, Xiong JG, He YL. Experimental and numerical study and comparison of performance for herringbone wavy fin and enhanced fin with convex-strips in fin-and-tube heat exchanger. Int J Heat Mass Transf. 2021;175(1):121390. doi:10.1016/j.ijheatmasstransfer.2021.121390.

28. Miao L, Wan R, Wu HW, Liu Z, Wang SS. Heat transfer and pressure drop characteristic research of sine wavy flying-wing fins. Sci Rep. 2023;13(1):15589. doi:10.1038/s41598-023-42872-x.
29. Sheng W, Fang YQ, Lan QY, Hao XR. Experimental study on the frosting characteristics and heat transfer performance of microchannel heat exchangers. J Refrig. 2021;42:89–98,110.
30. Yang SM, Tao WQ. Heat transfer. 4th ed. Beijing, China: Higher Education Press; 2006.
31. Li YY, Hu CR. Experimental design and data processing. 3rd ed. Beijing, China: Chemical Industry Press; 2017.
32. Yao X. Research on the improvement of signal-to-noise ratio of Taguchi method [master's thesis]. Changsha, China: Changsha University of Science and Technology; 2017.